Interplay of charge carrier and antiferromagnetic order in metallic triangular lattice $GdZn_3P_3$

Jiesen Guo,[1] Fan Yang,[1] Yuzhou He,[2] Xinyang Liu,[1,2,3] Zheng Deng,[2,4] Qinghua Zhang,[2,*] Xiancheng Wang,[2,4] Xianlei Sheng,[1,†] Wei Li,[3,5,6] Changqing Jin,[2,4] and Kan Zhao[1,‡]

[1]*School of Physics, Beihang University, Beijing 100191, China*

[2]*Beijing National Laboratory for Condensed Matter Physics, Institute of Physics, Chinese Academy of Sciences, Beijing 100190, China*

[3]*CAS Key Laboratory of Theoretical Physics, Institute of Theoretical Physics, Chinese Academy of Sciences, Beijing 100190, China*

[4]*School of Physical Sciences, University of Chinese Academy of Sciences, Beijing 1000190, China*

[5]*CAS Center for Excellence in Topological Quantum Computation, University of Chinese Academy of Sciences, Beijng 100190, China*

[6]*Peng Huanwu Collaborative Center for Research and Education, Beihang University, Beijing 100191, China*

(Received 16 July 2025; revised 19 December 2025; accepted 5 February 2026; published 25 February 2026)

We investigate a hexagonal $ScAl_3C_3$-type antiferromagnet $GdZn_3P_3$ single crystal. Compared with antiferromagnetic topological material EuM_2X_2 (M = Zn, Cd; X = P, As), the $GdZn_3P_3$ features an additional ZnP_3 trigonal planar units. Notably, single-crystal x-ray diffraction analysis reveals that Zn and P atoms within a trigonal planar layer exhibit significant anisotropic displacement parameters with space group $P6_3/mmc$. Meanwhile, a scanning transmission electron microscopy experiment demonstrates the presence of interstitial P atoms above and below the ZnP honeycomb lattice, suggesting potential ZnP bond instability within the ZnP_3 trigonal layers. Concerning the triangular Gd^{3+} layer, the magnetic susceptibility $\chi(T)$ and heat capacity measurements reveal an A-type antiferromagnetic order at $T_N = 4.5$ K. Below T_N, the in-plane $\chi(T)$ is nearly 4 times the $\chi(T)$ along c axis, indicative of strong magnetic anisotropy for salt-flux-grown $GdZn_3P_3$ crystal. The density function theory calculation shows that $GdZn_3P_3$ is an indirect semiconductor with a band gap 0.27 eV, supported by the resistivity measurement on the polycrystal sample. Interestingly, Hall measurements of metallic $GdZn_3P_3$ crystals grown via salt flux reveal a low concentration of hole carriers, consistent with the previously mentioned presence of interstitial P atoms. Furthermore, these crystals exhibit a pronounced nonlinear anomalous Hall effect below T_N. In contrast, $GdZn_3P_3$ crystals grown by chemical vapor transport display weak semiconducting behavior. Despite exhibiting a similar T_N, the in-plane $\chi(T)$ below T_N in the vapor-transport-grown crystal is approximately half in magnitude compared to that of the salt-flux-grown sample, which supports the hypothesis of charge carrier-mediated Ruderman-Kittel-Kasuya-Yosida interactions. These findings collectively establish $GdZn_3P_3$ as a compelling model system for investigating the coupling between charge carriers and triangular lattice magnetism within a two-dimensional framework.

DOI: 10.1103/qfbt-xn97

I. INTRODUCTION

Geometric frustration in magnetism has long been a prominent research focus in condensed matter physics, as this model prevents antiparallel spin alignment in the antiferromagnetic ground state. This results in significant entanglement and fluctuations, giving rise to many unique states, such as spin liquid [1–8], spin ice [9–16], and spin supersolid [17–20]. As the prototype model of the two-dimensional (2D) triangular lattice formed by rare earth ions has attracted more attention, notable examples include the quantum spin liquid candidate $YbMgGaO_4$ [3–8] and $ARCh_2$ (A = alkali or monovalent ions, R = rare earth, and Ch = O, S, Se) [21–24]. While most 2D triangular systems focus on insulators and the presence of itinerant electrons in the triangular lattice material, the emergence of exotic magnetic order could be driven by the Ruderman-Kittel-Kasuya-Yosida (RKKY) interactions.

Based on the above idea, hexagonal $ScAl_3C_3$-type RM_3X_3 (R = rare earth; M = Zn, Cd; X = P, As) compounds have been widely studied, with $P6_3/mmc$ space group [25–31]. As shown in Fig. 1(a), the crystal structure of RM_3X_3 features alternating layers of RX_6 octahedra, MX_4 tetrahedra, and MX_3 trigonal planar units, and the M_{trig} and X_{trig} atoms of MX_3 are cross arranged to form a honeycomb [26]. To compare, the antiferromagnetic topological materials EuM_2X_2 (M = Zn, Cd; X = P, As) crystallize in a trigonal system with the $P\bar{3}m1$ (No. 164) space group, constituting a layered structure composed of edge-sharing MX_4 tetrahedra and EuX_6 octahedra [32–45]. The interlayer distance between the triangular lattice layer of Eu^{2+} and Ce^{3+} ions increases from 7.1683 Å in $EuCd_2P_2$ and 7.3278 Å in $EuCd_2As_2$, to 10.2387 Å in $CeCd_3As_3$, which enhances the two-dimensional character of the RM_3X_3 structure. Previous studies of $CeCd_3X_3$ (X = P, As) have demonstrated strong easy-plane magnetic anisotropy explained by crystalline electric field (CEF) model [46], which demonstrated the low-carrier-density metallic state,

*Contact author: zqh@iphy.ac.cn
†Contact author: xlsheng@buaa.edu.cn
‡Contact author: kan_zhao@buaa.edu.cn

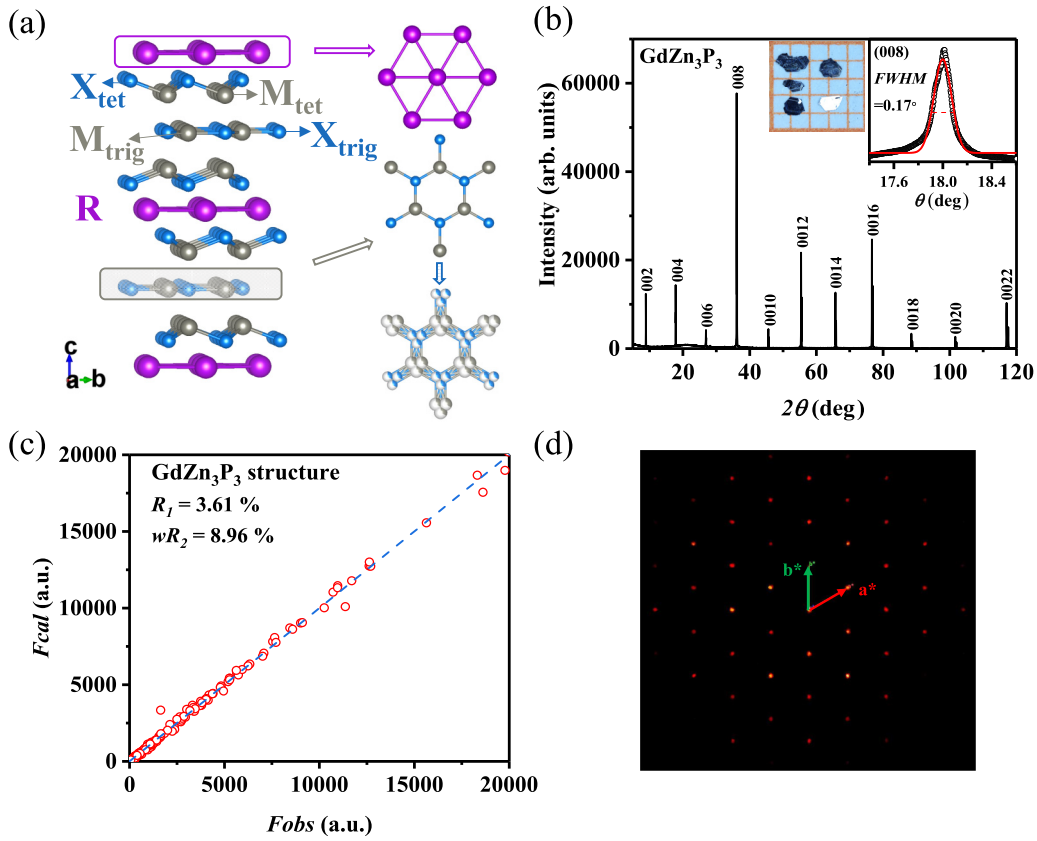

FIG. 1. (a) The crystal structure of RM_3X_3 (R = rare earth; M = Zn, Cd; X = P, As), with space group $P6_3/mmc$. Purple, grey, and blue spheres represent R, M, and X atoms, respectively. The triangular layer formed by R ions. The honeycomb network formed by MX_3 trigonal planar units, which M_{trig} and X_{trig} occupy 1, to the local distorted arrangement in which M_{trig} and X_{trig} are randomly distributed over three equivalent positions, respectively. (b) The XRD pattern of the $GdZn_3P_3$ (salt) single crystal, with the inset illustrating the rocking curve scan of the (008) peak fitted by Gaussian function, and a photograph of the single crystals also included. (c) Plots of calculated vs experimental structure factors for the refined structure at room temperature. (d) The diffraction spot pattern taken looking along the [001] from the single-crystal x-ray diffraction of $GdZn_3P_3$ (salt).

with antiferromagnetic (AFM) transitions at about 0.4 K [47,48]. In the $J_{eff} = 1/2$ compound $NdCd_3P_3$, the AFM transition temperature of 0.34 K is slightly lower than that of $CeCd_3X_3$ (X = P, As) [49,50], as well as this trend of magnetic transition being similar to that of RZn_3P_3 (R = rare earth) [29,51].

During the structural refinement within $P6_3/mmc$ space group, both Cd_{trig} and As_{trig} atoms of $CeCd_3As_3$ exhibit significantly large displacement parameters [26]. As reported in Ref. [26], this pathological issue can be partially removed by splitting atom positions or incorporating twins in a low-symmetry space group. Figure 1(a) illustrates an acceptable model that the Cd_{trig} and As_{trig} atoms are shifted from the ideal 2c and 2d sites (with –6m2 symmetry) to 6h sites (mm2 symmetry) at a partial occupancy of 1/3. Within the 6h sites, the 1/3 occupancy indicates the Cd and As atoms are randomly occupied in the three positions, forming a local distorted arrangement within the $CdAs_3$ trigonal planar layer. The scenario could be treated as a dynamic movement of Cd_{trig} acting on the surrounding As_{trig} atoms, which may cause the bond instability of $(CdAs)_{trig}$.

Recently, Ref. [52] provided direct evidence of the local distortion of CdP bonds associated with one-dimensional CdP chains in RCd_3P_3 (R = La, Ce, Pr, and Nd) single crystals, based on the observation of diffuse intensity in synchrotron x-ray diffraction (XRD) measurements. By mapping the Cd-P dimer covering problem onto a 2D Ising model defined on the dual triangular lattice, the effective interactions associated with the local bond order on the honeycomb lattice hinder the development of long-range order [52]. Therefore, the coexistence of bond instability and frustrated magnetism renders the RCd_3P_3 system particularly intriguing, as it extends the concept of geometrical frustration from solely encompassing the magnetic component of electrons to incorporating both spin and charge degrees of freedom. It is crucial to identify an isostructural compound with a relatively high magnetic transition temperature to easily investigate the interplay between the Cd/ZnP trigonal planar unit and magnetic triangular R^{3+} layer.

In this paper, we present the synthesis and characterization of isostructural $GdZn_3P_3$ single crystal. The ZnP bond instability within ZnP_3 trigonal planar units has been revealed through both single crystal x-ray diffraction (SCXRD) and scanning transmission electron microscopy (STEM) experiments. Based on the magnetic and thermodynamic data, we identify the ground state of $GdZn_3P_3$ as an A-type AFM order below $T_N = 4.5$ K. The $GdZn_3P_3$ system is calculated to be a semiconductor with a band gap of 0.27 eV by density

functional theory (DFT) method. During single-crystal growth, the incorporation of interstitial P atoms leads to hole doping in the $GdZn_3P_3$ system, significantly reducing its resistivity. This effect is evident in crystals grown via chemical vapor transport and ultimately results in metallic conductivity in salt-flux-grown crystals, accompanied by an anomaly at T_N. Thus, the metallic $GdZn_3P_3$ single crystal gives rise to the unique opportunity of investigating the emergent phenomenon in antiferromagnetic RM_3X_3 system, such as the observed nonlinear anomalous Hall effect related with the unconventional spin texture.

II. EXPERIMENTAL

The polycrystals of $CeCd_3As_3$ and $GdZn_3P_3$ were synthesized by the solid-state method. The CdAs, CdP, and ZnP precursors were first weighed in a glove box using a stoichiometric ratio of Cd powder (99.99%), As lump (99.99%), P lump (99.99%) and Zn powder (99.99%), then mixed in an agate mortar and sealed in an evacuated quartz tube. CdAs was sintered at 500 °C for 30 h, and CdP and ZnP were sintered at 250 °C for 30 h. CdAs and Ce (99.99%), CdP and Gd (99.99%), and ZnP and Gd were mixed at stoichiometric ratios and sintered. As shown in Figs. S1 and S2 in the Supplemental Material [53] (see also Ref. [54] therein), the phase pure $CeCd_3As_3$ and $GdZn_3P_3$ polycrystals have been successfully obtained under sintering at 700 °C for 30 h and 1100 °C for 30 h. Further details are provided in Supplemental Material Note 1 [53]. For transport measurements, the polycrystalline samples were pressed into pellets and subsequently sintered at 800 °C for 15 h.

High-quality single crystals of $GdZn_3P_3$ were grown by 0.5 g of stoichiometric amounts of Gd lump (99.99%), Zn powder (99.99%), and P lump (99.99%) together with 4 g of the NaCl/KCl (1:1) flux [25,29]. The sample was annealed for 24 h at 500 °C, followed by 170 h at 900 °C, then furnace cooled to room temperature. The platelike $GdZn_3P_3$ (salt) single crystals were collected by washing with deionized water.

High-quality single crystals of $GdZn_3P_3$ were also grown by the chemical vapor transport (CVT) method [30]. A mixture of stoichiometric amounts of Gd powder (99.99%), Zn powder (99.99%), and P powder (99.99%) totaling 0.5 g, together with 0.1 g of I_2 as the transport agent, was sealed in an evacuated quartz tube and placed in a two-zone horizontal furnace. The source and growth zones were maintained at 800° C and 700° C for 170 h. After furnace cooling to room temperature, hexagonal $GdZn_3P_3$ (CVT) single crystals were obtained as shown in Fig. S4.

XRD patterns were measured using a Bruker D8 ADVANCE diffractometer with Cu Kα ($\lambda = 1.5418$ Å) radiation at room temperature. The SCXRD data were performed using a Rigaku XtaLAB Synergy diffractometer at room temperature with the Mo Kα ($\lambda = 0.71073$ Å) radiation. The single crystal structure solution was completed using Olex2 [55] and SHELXL [56]. The high-angle annular-dark-field (HAADF) image and annular bright-field image were characterized using an ARM-200F (JEOL, Tokyo, Japan) scanning transmission electron microscope (STEM) operated at 200 keV with a CEOS Cs corrector (CEOS GmbH, Heidelberg, Germany) to cope with the probe-forming objective spherical aberration. The magnetic properties were measured using the Quantum Design Magnetic Property Measurement System (MPMS). The specific heat was measured using the Quantum Design Physical Property Measurement System (PPMS). The resistivity and Hall data was measured using the Cryogen Free Measurement System.

TABLE I. Crystal data and structure refinement for single-crystal $GdZn_3P_3$ (salt).

Formula	$GdZn_3P_3$
T(K)	293(2)
Crystal system	Hexagonal
Space group	$P6_3/mmc$
a(Å)	4.0107(3)
b(Å)	4.0107(3)
c(Å)	19.8808(15)
V(Å)^3	276.95(4)
θ	2.049–28.158
No. reflections collected	1066
No. of variables	14
Final R indices	$R_1 = 0.0361$, w$R_2 = 0.0896$
R indices (all data)	$R_1 = 0.0405$, w$R_2 = 0.0911$
Goodness of fit	0.992
Largest diff. peak and hole (eÅ^{-3})	0.92, –1.09

Our DFT uses the generalized gradient approximation (GGA) [57,58] in the form of PBE functional [59] and included spin-orbit coupling, as implemented in the Vienna ab initio Simulation Package [60–62]. The energy cutoff of the plane-wave basis is set to 350 eV. The energy convergence criterion in the self-consistent calculations is set to 10^{-6} eV. A $9 \times 9 \times 3$ $\Gamma-$centered Monkhort-Pack k-point mesh is used for the first Brillouin zone sampling. To account for the correlation effects for Gd, we adopted the GGA + U method with the value of $U = 1$ eV.

III. RESULTS AND DISCUSSION

A. Crystal structure of $GdZn_3P_3$ (salt) single crystal: X-ray diffraction and STEM analysis

A series of (0, 0, 2L) peaks are observed by XRD diffraction experiment in Fig. 1(b), indicating the *ab* plane as the natural cleavage plane. Rocking curve analysis of the Bragg peak (008) in the inset of Fig. 1(b) demonstrates a narrow full width at half maximum of 0.17°, indicating high quality of the $GdZn_3P_3$ crystals. The single crystal diffraction spots along [001] in Fig. 1(d) show direct evidence for the six-degree symmetry of hexagonal $GdZn_3P_3$ system, with related spots along [100] and [010] shown in Fig. S5 [53]. The Rietveld refinements of the SCXRD data converge to the agreement factors $R_1 = 3.61\%$ and $wR_2 = 8.96\%$ in Fig. 1(c), with $a = b = 4.0107(3)$ Å and $c = 19.8808(15)$ Å in Table I. The corresponding crystal structure is depicted in Fig. 2(c), with the refined atomic parameters listed in Table II.

Due to the presence of large voids above and below the location in Fig. 2(c), Zn_{trig} atom exhibits large anisotropic displacement parameters, with $U_{33} = 0.048$ along the c axis and $U_{11} = 0.032$ in the *ab* plane at room temperature. These

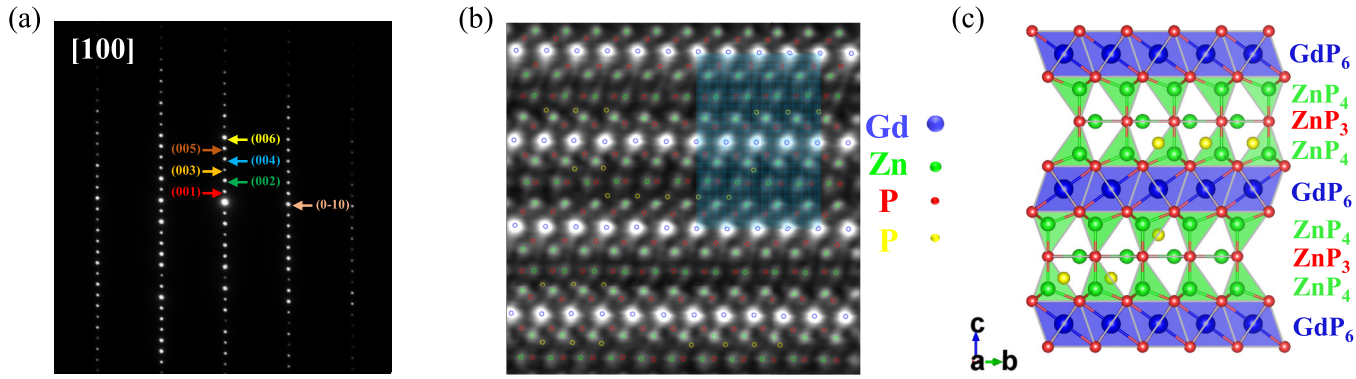

FIG. 2. (a) The electron diffraction pattern along [100] direction. (b) The high-angle annular dark-field (HAADF) image of $GdZn_3P_3$ (salt) taken along [100] direction. The blue, green, red, and yellow spheres represent Gd, Zn, P, and the interstitial impurity P, respectively. (c) Corresponding crystal structure of $GdZn_3P_3$ (salt) along [100] direction, matching the blue-boxed region in Fig. 2(b). The structure features alternating layers of GdP_6 octahedra, ZnP_4 tetrahedra, and ZnP_3 trigonal planar units, with the yellow ball marks the anticipated site of the interstitial P atom.

values are comparable to the values of 0.0501 and 0.02826 for Cd_{trig} atoms of $PrCd_3P_3$. On the other hand, the P_{trig} atom has larger in-plane displacement with the U_{11} parameter as 0.031, also comparable with the value of 0.0392 for P_{trig} atoms of $PrCd_3P_3$ [52].

To reveal the structural details of interlayer atoms in atomic scale, we continue to perform STEM on a *bc* plane of $GdZn_3P_3$ about $4 \times 3\,\mu m^2$ area, with details information in Fig. S6 [53,63]. As shown in Fig. 2(a), the selected area electron diffraction pattern contains a series of diffraction peaks, such as (001), (002), (003), and (004), etc., and (0–10). Moreover, the HAADF image in Fig. 2(b) directly shows the atomic arrangement in the unit cell of $GdZn_3P_3$ projected along the [100] direction, corresponding to the crystal structure in Fig. 2(c). First, the HAADF image confirms the full occupancy of Zn_{trig} and P_{trig} atoms within the ZnP_3 trigonal planar. We conclude that the underlying bond instabilities of $(ZnP)_{trig}$ are local characteristics rather than uniform.

Notably, numerous interstitial P atoms are observed in the HAADF image, as indicated by the yellow spheres in Fig. 2(b). Within the honeycomb lattice of Zn_{trig} and P_{trig} atoms, the bond distance is about 2.32 Å, while the distance between Zn_{trig} and P_{tet} atom is 3.29 Å along the *c* axis. Thus, the presence of interstitial P atom is closely related with the large voids above and below the location of Zn_{trig} atoms in Fig. 2(c). The estimated occurrence probability of interstitial P atoms per formula unit (f. u.) is inferred from a statistical analysis of multiple spatial regions during the STEM measurement. Specifically, approximately 24 interstitial P atoms are observed in 44 formula units in the projection plane along the [100] direction in Fig. 2(b), corresponding to ~0.55 per f. u., while 18 and 17 interstitial P atoms are observed in 44 formula units along the [100] direction in Figs. S7(a) and S7(b), corresponding to ~0.41 and ~0.39 per f. u., respectively. On this basis, the interstitial P atoms projected along [100] direction appear with an average probability of ~0.45 per f. u.

By combining the two orthogonal projections along and perpendicular to the [100] direction, an average volumetric probability of approximately 0.2 (0.45×0.45) is obtained. Taking into account that the weak image contrast of an interstitial P atom is ~ 0.2 of that of a regular P site, the resulting volumetric density is estimated to be ~0.04 (0.2×0.2) per f.u. Such a low concentration is well below the detection limit of x-ray diffraction, with no corresponding signatures observed in XRD patterns of Fig. 1. And we will discuss the effect of interstitial P atoms in electronic transport section later.

Recently, the structural instability within ZnP/As honeycomb layer has been revealed in its sister compound $GdZn_3As_3$ [31], which crystallizes in a distorted $ScAl_3C_3$-type orthorhombic structure with *Cmcm* space group, analogous to the case of $YbAl_3C_3$ [64]. It warrants performing the synchrotron x-ray diffraction measurement to investigate the potential existence of short-range bond order existing in RZn_3P_3 (R = La, Ce, Pr, Nd and Gd) single crystals in future research.

TABLE II. Wyckoff positions, atomic coordinates, occupancies, isotropic and anisotropic displacement parameters (Å^2), where $U_{23} = U_{13} = 0$ for $GdZn_3P_3$ (salt).

Atom.	Wyck.	x	y	z	Occup	U(eq)	U_{11} (U_{22})	U_{33}	U_{12}
Gd	2*a*	0	0	0.5	1	0.0095(5)	0.0075(6)	0.0134(8)	0.0038(3)
Zn_{tet}	4*f*	–1/3	1/3	0.6299(1)	1	0.0136(7)	0.0139(9)	0.0130(11)	0.0069(5)
Zn_{trig}	2*d*	–2/3	2/3	3/4	1	0.0374(13)	0.0321(19)	0.048(3)	0.0160(9)
P_{tet}	4*f*	2/3	1/3	0.4155(3)	1	0.0112(12)	0.0117(17)	0.010(2)	0.0058(8)
P_{trig}	2*c*	–1/3	1/3	3/4	1	0.024(2)	0.031(4)	0.011(4)	0.0153(18)

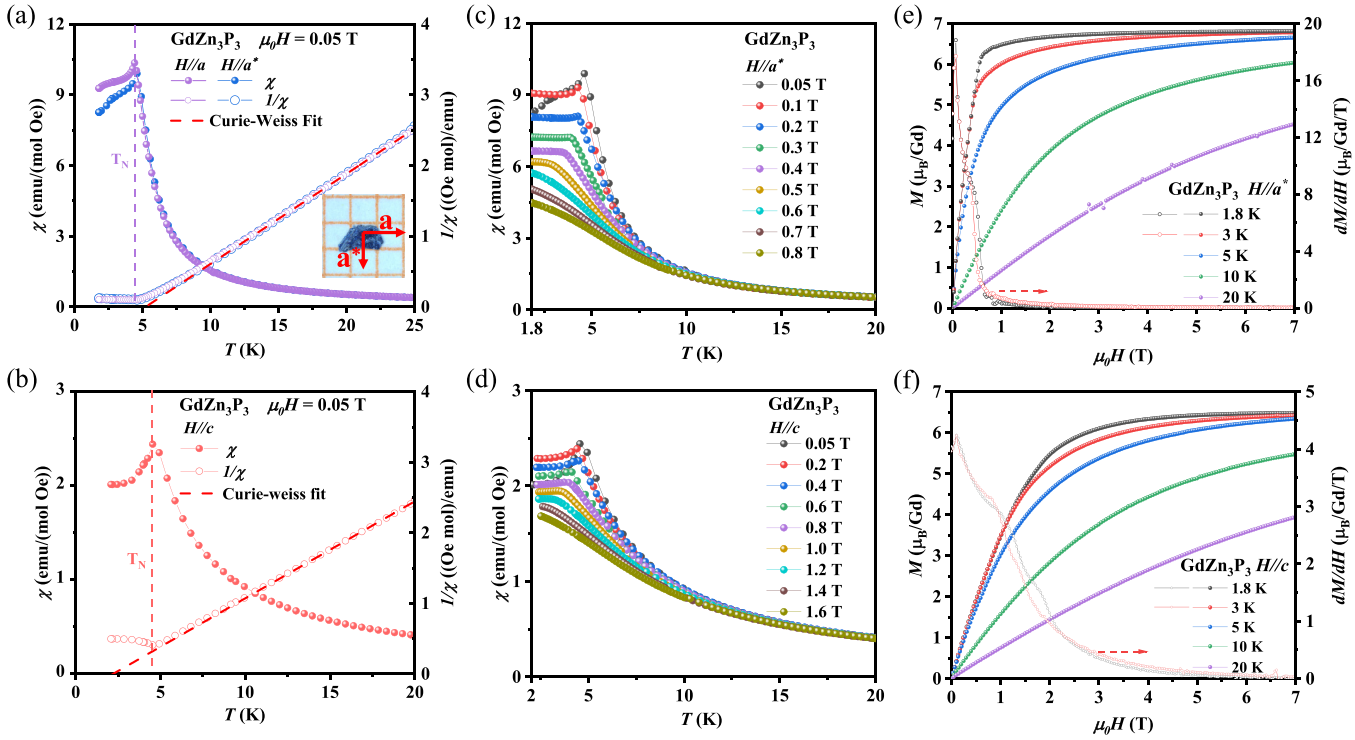

FIG. 3. (a), (b) The temperature-dependent magnetic susceptibility $\chi(T)$ of $GdZn_3P_3$ (salt) between 1.8 and 25 K measured with magnetic field along a, a^*, and c directions, an inset optical image of the single crystal. (c), (d) The $\chi(T)$ below 20 K at various fields along a^* and c directions. (e), (f) Isothermal magnetization $M(H)$ and the differential susceptibility dM/dH at different temperatures with the magnetic field applied along the a^* and c directions.

B. Magnetic properties and magnetic structure of $GdZn_3P_3$ (salt) single crystal

Magnetic susceptibility $\chi(T)$ measurements of $GdZn_3P_3$ have been performed under magnetic field along a, a^*, and c axes, showing a clear AFM transition at $T_N = 4.5$ K, as shown in Figs. 3(a) and 3(b) and Figs. S8–S9 [53]. The $\chi(T)$ curve exhibits no significant difference between a and a^* directions, with its value being about 4 times that along the c axis below T_N. In Fig. S9(a), the Curie-Weiss law is used to fit the $\chi(T)$ (200–300 K) under 0.05 T, yielding $\mu_{\text{eff}} = 7.93\,\mu_B$/Gd in the ab plane, consistent with the expected value $7.94\,\mu_B$. In Figs. 3(a) and 3(b), the Curie-Weiss law is used to fit the $\chi(T)$ from 15–25 K for $H \parallel a$ and from 15–20 K for $H \parallel c$, which yields $\theta_{\text{CW}} = 5.2$ K for $H \parallel a^*$, and $\theta_{\text{CW}} = 2.0$ K for $H \parallel c$.

These characteristics suggest the formation of an A-type AFM order, likely with the spin alignment of Gd^{3+} ions lying in the ab plane below T_N and FM layers stacked antiferromagnetically. From the perfect hexagonal structure to the distorted $ScAl_3C_3$-type case, accompanied by the release of magnetic frustration, the ground state evolves from A-type AFM order with $T_N = 4.5$ K in $GdZn_3P_3$ to FM order with $T_c = 6.3$ K in $GdZn_3As_3$ [31].

Similarly, A-type AFM order has also been observed in topological material EuM_2X_2 (M = Zn, Cd; X = P, As), with T_N at about 23 K in $EuZn_2P_2$ [40–42,44,45] and 9.3 K in $EuCd_2As_2$. The much lower T_N in $GdZn_3P_3$ is speculated to be largely due to the extra honeycomb nets ZnP layer between triangular lattice of Gd atoms, thus weakening the AFM interaction strength. According to the previous literature, the magnetic moments of $EuCd_2As_2$ and $EuZn_2As_2$ are determined to be parallel to ab-plane through resonant elastic x-ray scattering (REXS) and neutron diffraction; and the spins of $EuZn_2P_2$ are canted out of the a-a plane by an angle of about $40° \pm 10°$ and aligned along the [100] direction as confirmed by resonant magnetic x-ray diffraction data [32,39,40,42].

We also note a subtle cusp appears in the ab-plane $\chi(T)$ curve at 2.4 K [see Fig. 3(a) and Fig. S8], and to capture this feature, Fig. S8(a) displays the temperature derivative of $\chi(T)$ ($d\chi/dT$) curve. A modulated magnetic order observed in GdV_6Sn_6 indicates the presence of an incommensurate magnetic order below 5.2 K and a commensurate magnetic order below 3.8 K, as demonstrated by REXS measurements [65,66]. To clarify the microscopic magnetic structure together with its temperature dependence of $GdZn_3P_3$, it seems necessary to conduct REXS and neutron scattering measurements in future.

In addition, the $\chi(T)$ curves at different magnetic fields were measured as shown in Figs. 3(c) and 3(d). With the magnetic field increased to 0.6 T for $H \parallel a^*$ and 1.4 T for $H \parallel c$, the AFM transition peak has been completely suppressed to below 1.8 K for $H \parallel a^*$ and 2.5 K for $H \parallel c$. The corresponding $d\chi/dT$ curves are presented in Fig. S9 [53]. As shown in Figs. 3(e) and 3(f), the magnetization saturates at $M_S \sim 6.7\,\mu_B$ for $H \parallel a^*$ and $M_S \sim 6.5\,\mu_B$ for $H \parallel c$ at 1.8 K, consistent with the expected value $7\,\mu_B$ for Gd^{3+} ions. The transition fields are determined from the dM/dH curves in Fig. 3(e) as $\mu_0 H_{ab} = 0.6$ T at 1.8 K and 0.5 T at 3 K for $H \parallel a^*$, respectively. For a detailed description of the determination process of the metamagnetic transitions under $H \parallel c$,

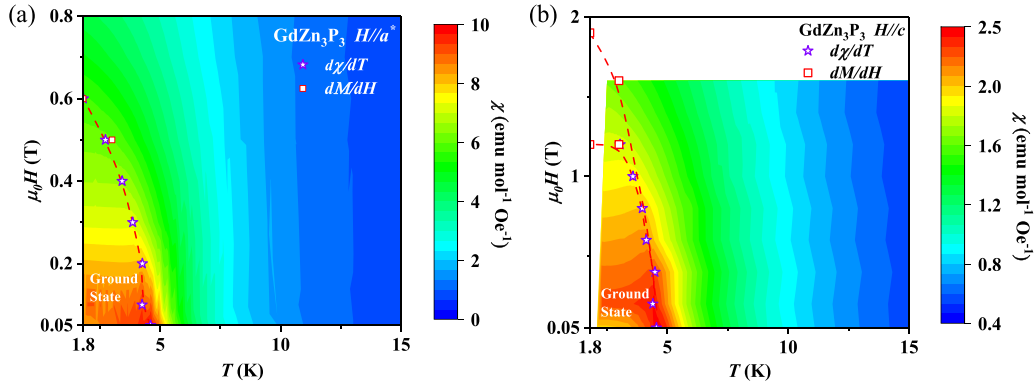

FIG. 4. (a), (b) The *H-T* magnetic phase diagram overlaid on the contour plots of the magnetic susceptibility of $GdZn_3P_3$ (salt) with the field along the a^* and c directions, respectively. The magnetic phase boundaries were extracted through $\chi(T)$ and $M(H)$ measurements. The star and square symbols, respectively, denote the temperature at a specific field where these transition peaks are observed in the temperature derivative of susceptibility $d\chi/dT$ and the differential susceptibility dM/dH. The dashed lines represent the magnetic phase boundary.

please refer to Fig. 9(d). Finally, Figs. 4(a) and 4(b) depict the *H-T* phase diagram constructed by combining the AFM transition peaks obtained above.

C. Magnetic heat capacity and entropy of $GdZn_3P_3$ (salt) single crystal

Figure 5 presents the temperature dependence of the measured heat capacity C_p curve, which reveals a sharp transition close to $T_N = 4.5$ K. The temperature dependence of the specific heat of $LaZn_3P_3$ in zero magnetic field was taken from Ref. [51] and is shown in Fig. 5(a), where the background phonon contribution is fitted by a polynomial expression $C_{ph} = aT^3 + bT^5 + cT^7 + dT^9 + eT^{11}$ [67,68]. The magnetic heat capacity C_m is obtained after subtracting phonon contribution. There is still residual magnetic entropy below 1.8 K, so the lower temperature magnetic heat capacity is fitted through the power law $C_m(T) = b \times T^a$ to get a = 1.16 as shown in Fig. 5(b), which does not follow the $C_m(T) \sim T^3$ relation observed in the conventional ungapped AFM magnon excitations [69]. By integrating $(C_p - C_{ph})/T$ from 15 K to 0 K, the obtained values of the magnetic entropy S_{mag} are 15.9 J/(mol K),which is 92% of the expected magnetic entropy as *Rln8*. The heat capacity C_p data below 1.8 K seems necessary to obtain a more accurate power law fitting as well as the integrated S_{mag} value.

D. Electronic band structure DFT calculation and transport results of polycrystalline $GdZn_3P_3$

Similar to the $EuCd_2As_2$ case [36], $GdZn_3P_3$ may have three possible A-type AFM structures, as shown in Fig. 6(a), with magnetic moments of Gd^{3+} ions along b, c, and x directions, and the configuration with the moment aligned along the b axis exhibits the lowest free energy according to DFT calculations. Given the magnetic evidence above, the ground state of $GdZn_3P_3$ would most likely be A-type magnetic structure with Gd moment along the b axis (i). Figures 6(b) and S11 display the corresponding band structures with spin-orbit coupling included and density of states (DOS) plot near

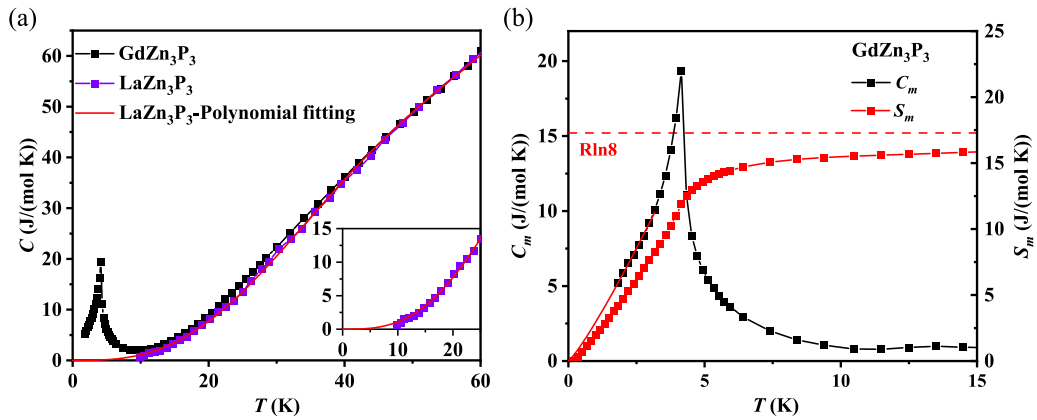

FIG. 5. (a) Temperature-dependent specific heat of $GdZn_3P_3$ (salt) (black square) of $LaZn_3P_3$ (from Ref. [51]) (purple square), The dashed red line represents a polynomial fit temperature-dependent specific heat of $LaZn_3P_3$ to estimate the lattice contribution. The inset shows an enlarged view of the specific heat of $LaZn_3P_3$ polynomial fitting below 25 K and an inset photo of the single crystal of $GdZn_3P_3$ (salt) for heat capacity measurement in the PPMS puck. (b) The C_m (black line) with the portion of the zero field $C_m(T)$ fitted to a $b \times T^a$ power law (red extension line) and temperature-dependent integrated magnetic entropy (red line).

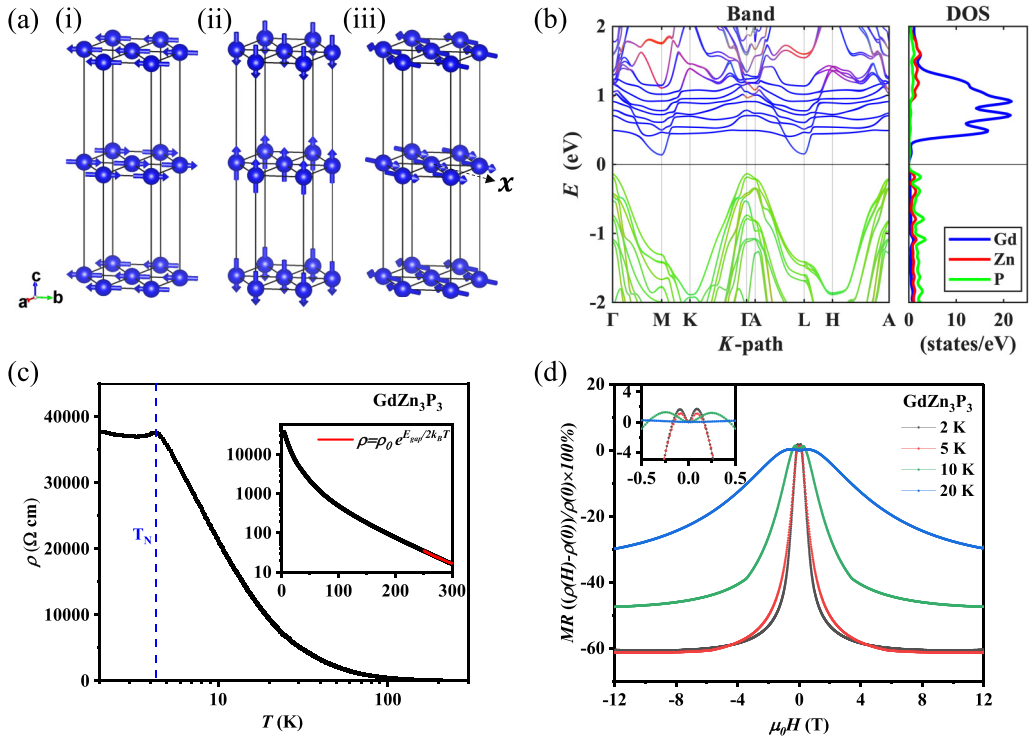

FIG. 6. (a) Proposed possible magnetic structure of $GdZn_3P_3$. A-type AFM structure configurations on Gd sites with the magnetic moment aligned along *b* (i), *c* (ii), or *x* (iii) directions. (b) (i) corresponding Band structure with spin-orbit coupling included and density of states (DOS) plot near the Fermi level, calculated via density functional theory (DFT). (c) The temperature-dependent resistivity of polycrystalline $GdZn_3P_3$ sample between 2 K and 300 K, with the inset showing the transport activation gap extracted from a fit in the 250–300 K range. (d) Magnetoresistance (MR) of $GdZn_3P_3$ as a function of field at several representative temperatures, with the inset revealing the detailed behavior of MR in the field range of −0.5 T to 0.5 T.

the Fermi level, with indirect band gaps from Γ to *M* as 0.27 eV, 0.28 eV, and 0.26 eV, respectively [53]. This band gap is smaller than that of polycrystalline $LaCd_3P_3$ (0.75 eV) and $NdCd_3P_3$ (0.63 eV). In addition, the indirect band gap of $EuZn_2P_2$ is calculated to be 0.2 eV, and observed as 0.09 eV in the angle-resolved photoemission spectroscopy experiment [42].

Figure 6(c) illustrates the electrical resistivity of polycrystalline $GdZn_3P_3$ within the temperature range 2–300 K, consistent with the semiconducting behavior observed in RCd_3P_3 (R = La, Ce, and Nd) polycrystals. As depicted in inset of Fig. 6(c), the transport gap of $GdZn_3P_3$ is extracted from a fit to the resistivity data between 250 and 300 K using the thermally activated Arrhenius form $\rho = \rho_0 e^{E_{\rm gap}/2k_BT}$, yielding a band gap of approximately 0.2 eV, consistent with the DFT calculation results above. Interestingly, the AFM transition also shows up in the resistivity curve, marked as $T_N = 4.5$ K in Fig. 6(c). A similar characteristic has also been observed in $EuZn_2P_2$ and $EuCd_2As_2$ [21,51].

As shown in inset of Fig. 6(d), the magnetoresistance (MR) curve below 20 K exhibits an initial increase under small field ($\mu_0 H < 0.3$T), which may be associated with the impurity carriers—similar behavior also reported in $EuZn_2As_2$ [43]. Under high field, the magnetic scattering would be suppressed in the polarized FM state, thus a negative MR has been observed in polycrystalline $GdZn_3P_3$ under field up to 12 T. According to Figs. 3(e) and 3(f), the $GdZn_3P_3$ compound enters the polarized state under 1 T for $H \parallel a^*$ and 4 T for $H \parallel c$. Thus, the negative MR below 5 K quickly reaches a magnitude of –60% under 4 T, then saturates at this value under $\mu_0 H > 4$T. The magnitude of negative MR in $GdZn_3P_3$ is compared to that of $EuZn_2As_2$ [43], $EuZn_2P_2$, and $EuCd_2As_2$ [21,49]. The MR curve becomes more pronounced as temperature decreases from 20 K to 2 K, indicating the significant influence of magnetic ordering behavior on the electronic transport properties in $GdZn_3P_3$.

E. Electronic transport of the $GdZn_3P_3$ (salt) single crystal

Figure 7(a) illustrates the in-plane resistivity curve of $GdZn_3P_3$ (salt) single crystal, exhibiting metallic behavior at elevated temperatures. Below 50 K, the resistivity slightly increases with cooling, and arising from enhanced magnetic scattering below 10 K, the resistivity rapidly increases to its peak value around $T_N = 4.5$ K. The resistivity value herein is on the order of 1 mΩ cm, consistent with the case of $GdZn_3As_3$ single crystal [31].

Figures 7(b) and 7(c) summarize field-dependent MR data from 2 K to 20 K under $H \parallel ab$ and $H \parallel c$, respectively. It is clear that the negative MR along two directions obtains its maximum value as the temperature approaches T_N. At $T = 2$ K, the negative MR curve quickly reaches the polarized state under 1 T for $H \parallel ab$ and 4 T for $H \parallel c$, consistent with the transitions observed in the *M(H)* curves [Figs. 3(e) and 3(f)]. Both in-plane and out-of-plane MRs reach approximately 40%, which is smaller than that observed in the

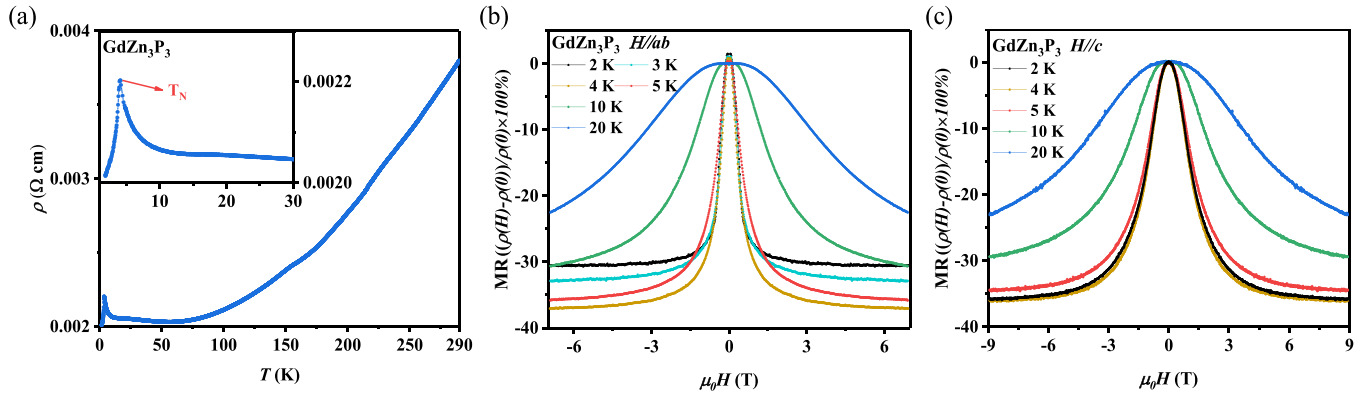

FIG. 7. (a) The temperature-dependent resistivity of single crystal $GdZn_3P_3$ (salt), with the inset revealing the detailed behavior of resistivity below 30 K. (b), (c) Magnetoresistance (MR) of $GdZn_3P_3$ (salt) as a function of field applied within the *ab* plane and along the *c* axis at several representative temperatures.

polycrystalline sample due to enhanced magnetic and grain-boundary scattering in the latter.

The metallic conductivity of $GdZn_3P_3$ (salt) single crystal enables the Hall measurement down to low temperatures. We note the Hall data presented in Fig. 8 exhibits larger noise to signal ratio compared with the MR curves in Fig. 7 due to the relatively high contact resistance and thin thickness in the salt-flux grown crystals, as mentioned in $GdZn_3As_3$ case as well. In the latter, the Hall data was only obtained down to 10 K with acceptable quality.

At 50 K and 80 K, the Hall resistivity of $GdZn_3P_3$ shows a positive slope as a function of field, indicating hole-type carriers. The carrier concentration, obtained from linear fits to the Hall data, is approximately 1×10^{19} cm^{-3} and 1.3×10^{19} cm^{-3}, corresponding to 1.4×10^{-3} and 1.8×10^{-3} holes per f.u., comparable to $CeCd_3P_3$ ($\sim 2 \times 10^{-3}$ holes per f.u.) [47], and $GdZn_3As_3$ ($\sim 2.3 \times 10^{-3}$ holes per f.u.) [31]. It should be noted that the interstitial P atoms occupy nonstandard positions within the hexagonal $ScAl_3C_3$-type crystal structure. Consequently, it is unlikely that all interstitial P atoms with volumetric density roughly 0.04 per f.u. serve as effective dopants contributing free carriers to the band structure of semiconducting $GdZn_3P_3$. The observed hole-type conductivity in $GdZn_3P_3$ single crystal is therefore attributed to the presence of interstitial P atoms, consistent with the Hall effect measurements presented above.

The Hall resistivity exhibits a nonlinear dependence on the magnetic field at 20 K, and an additional humplike feature appears at $T = 3$ K, below T_N. This behavior gradually disappears as $GdZn_3P_3$ approaches saturation state under $\mu_0 H > 4$ T, which typically originates from nonzero Berry curvature induced by finite scalar spin chirality within magnetic domain walls. This phenomenon, known as the nonlinear AHE, has been observed in topological candidate materials $EuCd_2As_2$ and $EuZn_2Sb_2$ [37,70], as well its sister compound $GdZn_3As_3$ [31].

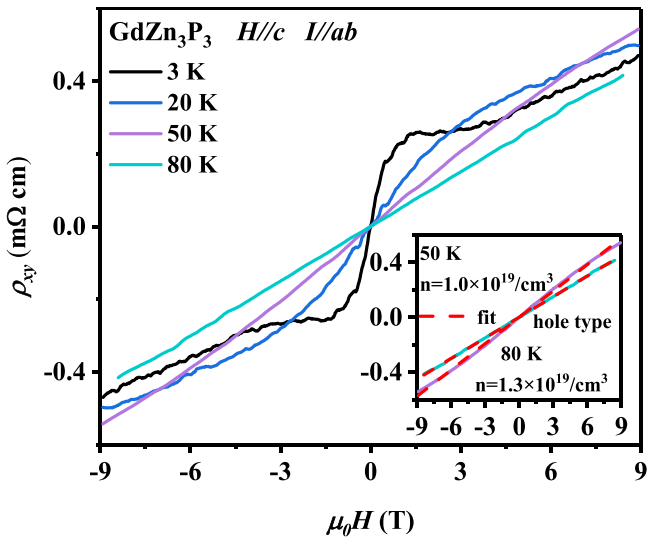

FIG. 8. Magnetic field dependence of the Hall resistivity (ρ_{xy}) for the single crystal $GdZn_3P_3$ (salt) at various temperatures (3, 20, 50, and 80 K). The inset displays linear fits to the Hall resistivity data at 50 K and 80 K.

F. Physical property of the $GdZn_3P_3$ (CVT) single crystal

As mentioned above, the resistivity values of $GdZn_3P_3$ (salt) crystal are on the order of 1 mΩ cm, significantly lower than the 10 mΩ cm value previously reported for $GdZn_3P_3$ single crystals in Ref. [29]. According to our Hall measurement, the different resistivity value might be caused by the different density of hole type carriers and interstitial P atoms.

To explore the coupling between charge carrier and antiferromagnetism in $GdZn_3P_3$, we continue to grow $GdZn_3P_3$ crystal with the CVT method, and characterize its physical property below. As depicted in Fig. 9(a), the $GdZn_3P_3$ (CVT) single crystal shows weak semiconducting behavior, with the resistivity value increasing from 27 mΩ cm at 300 K to 0.7 Ω cm at 2 K. Despite exhibiting a similar T_N, the magnitude of $\chi(T)$ along the *a* axis below T_N in Fig. 9(b) is approximately half that of the $GdZn_3P_3$ (salt) sample, while the value along the *c* axis is slightly lower than that of latter crystal. In Fig. 9(b), the Curie-Weiss fitting of $\chi(T)$ (15–25 K) yields $\theta_{CW} = 4.1$ K for $H \parallel a$ and $\theta_{CW} = 1.6$ K for $H \parallel c$, which are comparable to the $GdZn_3P_3$ (salt) case. Notably, the anomaly observed in the in-plane $\chi(T)$ curves of the salt-flux-grown

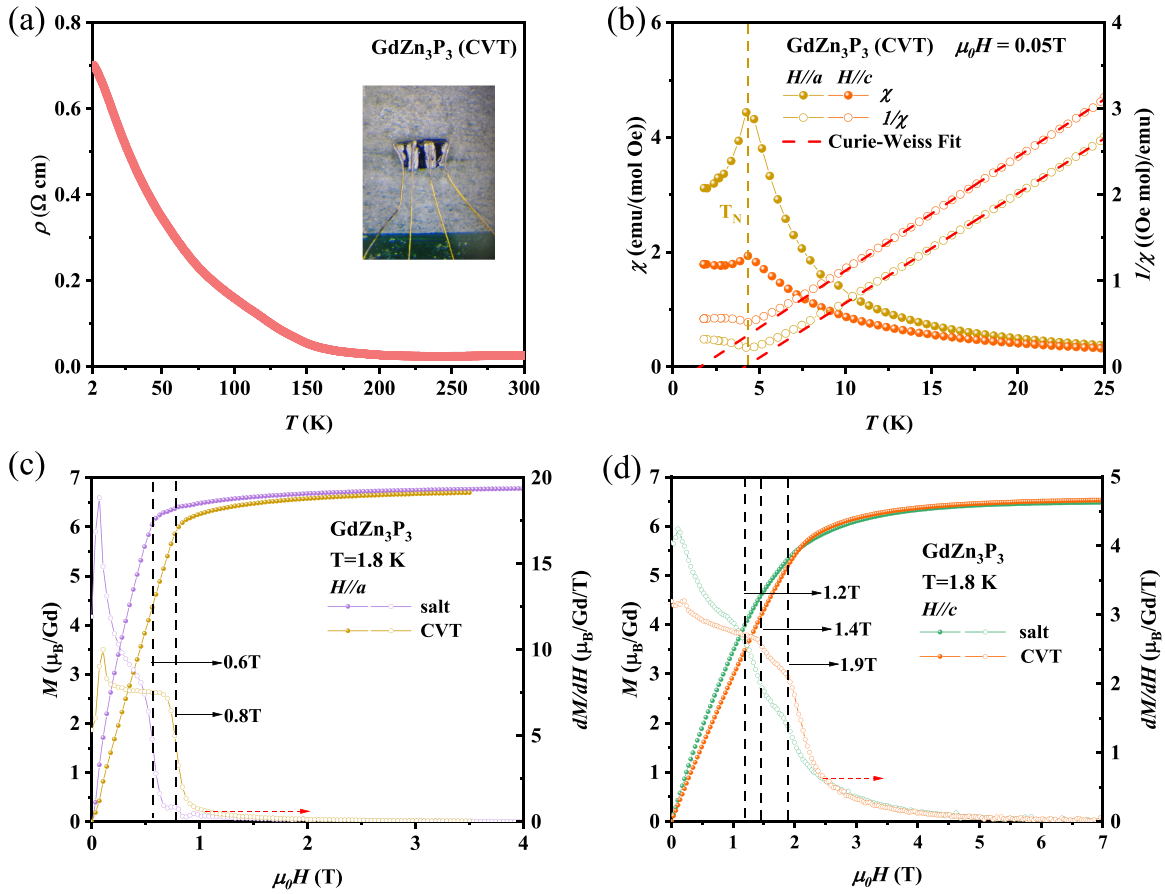

FIG. 9. (a) The temperature-dependent resistivity of $GdZn_3P_3$ (CVT) single crystal between 2 K and 300 K. (b) The temperature-dependent magnetic susceptibility $\chi(T)$ of $GdZn_3P_3$ (CVT) single crystal between 1.8 and 25 K measured with magnetic field along a and c directions. Isothermal magnetization and the differential susceptibility dM/dH at 1.8 K with the magnetic field applied along the a (c) and c (d) directions for $GdZn_3P_3$ (salt) and $GdZn_3P_3$ (CVT) single crystals.

crystal below 3 K is absent in the CVT-grown sample (see Fig. S12).

The saturated magnetization reaches $M_S \sim 6.7\,\mu_B$ for $H \parallel a$ and $M_S \sim 6.5\,\mu_B$ for $H \parallel c$ at 1.8 K [Fig. 9(c) and 9(d)], consistent with the values observed in $GdZn_3P_3$ (salt). From the corresponding dM/dH curves shown in Fig. 9(d), the metamagnetic transition for $H \parallel a$ occurs at approximately $\mu_0 H_{ab} = 0.8$ T, which is higher than the in-plane transition field of $\mu_0 H_{ab} = 0.6$ T observed in $GdZn_3P_3$ (salt). For $H \parallel c$, the metamagnetic transition field at $\mu_0 H_{c1} = 1.4$ T is higher than the $\mu_0 H_{c1} = 1.2$ T observed in $GdZn_3P_3$ (salt), and both samples exhibit another metamagnetic transition near $\mu_0 H_{c2} = 1.9$ T. Finally, the two curves are on top of each other above 2.5 T. In addition, small anomalous features have also been observed near zero field for both in-plane and out-of-plane orientations in Figs. 9(c) and 9(d), the microscopic origin of which requires further investigation.

The resistivity of the $GdZn_3P_3$ (CVT) crystal at 300 K is measured to be 27 mΩ cm, which lies between the values observed for the polycrystalline sample (20 Ω cm at 300 K) and the salt-grown crystal (4 mΩ cm at 290 K). It is noteworthy that the magnitude of low-temperature $\chi(T)$ for $GdZn_3P_3$ (CVT) single crystal is basically comparable to that observed in $GdZn_3P_3$ single crystals reported in Ref. [29]. Moreover, both crystals exhibit comparable resistivity values at 300 K and are situated within the semiconductor-to-metal transition region. In contrast to the single crystals in Ref. [29], whose resistivity gradually decreases with decreasing temperature, the $GdZn_3P_3$ (CVT) single crystal exhibits weak semiconducting behavior, as previously noted.

The metallic conductivity observed in the $GdZn_3P_3$ (salt) single crystal is likely attributable to the relatively high carrier density introduced during crystal growth. Through the RKKY exchange interaction, the charge carriers may also influence the magnetic properties, such as enhancing the magnetic anisotropy in this $S = 7/2$ Gd^{3+}-containing system. Correspondingly, the anisotropy factor $\chi_a(T)/\chi_c(T)$ at T_N increases from 2.3 in the semiconducting CVT-grown sample to 4.2 in the metallic salt-flux grown sample. Consequently, our investigation of the physical properties of both salt-flux-grown and CVT-grown $GdZn_3P_3$ crystals, combined with a comparative analysis of the results from Ref. [29], clearly demonstrates that the A-type AFM ordering of Gd^{3+} ions origins from the RKKY interaction mediated by hole-type carriers.

Such intriguing behavior has also been observed in topological materials $EuCd_2As_2$, where both metallic salt-flux-grown crystal and semiconducting Sn-flux-grown crystal exhibit A-type antiferromagnetic transitions at $T_N \sim 9.3$ K [34,35,38]. Under $H \parallel c$, the magnitude of $\chi(T)$

of $EuCd_2As_2$(Sn) (∼2.5 emu/mol) is smaller than that of $EuCd_2As_2$(salt) (∼4 emu/mol), while for $H /\!\!/ ab$, the magnitude of $\chi(T)$ of $EuCd_2As_2$(Sn) (∼5 emu/mol) is about half that of $EuCd_2As_2$(salt) (∼12 emu/mol) below T_N. According to Ref. [34], further Eu vacancies would drive the $EuCd_2As_2$ system into metallic FM state below $T_C = 26.4$ K.

IV. DISCUSSION AND CONCLUSION

For the magnetic topological system $EuMnSb_2$ [71–73] and $EuCd_2As_2$ [34], both materials exhibit narrow-gap semiconductor behavior. The presence of vacancies at Eu sites can introduce hole-type charge carriers and lead to metallic conductivity within the system. Concurrently, the enhanced RKKY interaction between the Eu magnetic moments and these charge carriers slightly alter the temperature-dependent magnetic ordering behavior, resulting in modifications to the spin configuration in the ground-state.

According to Ref. [49], the RCd_3P_3 would be semiconductor with a band gap between 0.6–0.8 eV, verified by the DFT calculation and the polycrystal results. Given the narrow band gap of the RCd_3P_3 family, these compounds are likely dopable into a metallic state as well. According to previous research, single crystals of RCd_3X_3 (R = La, Ce; X = P, As) exhibit metallic behavior, with the resistivity on the order of 10 mΩ cm (1 mΩ cm) for P (As) compounds [47,48], yet the exact origin still unclear.

Here, the ZnP bond instability in $GdZn_3P_3$ has been demonstrated through both x-ray diffraction and STEM measurement. Our atomic resolution STEM measurement reveals the presence of interstitial P atoms close to the ZnP honeycomb lattice, which would act as electron acceptors, thereby introducing hole-type carriers into the semiconducting system. Our investigation gives important insight into the metallic behavior of RZn_3P_3 and RCd_3X_3 (R = La, Ce; X = P, As) single crystals, thus it would be interesting to conduct the STEM measurement on the above single crystal to reveal its origin in atomic scale.

As mentioned above, the structural instability in ZnP layer could influence the rare-earth magnetic ion triangular layer through the charge carrier mediated RKKY magnetic interaction as observed in $GdZn_3P_3$; meanwhile, the influence could also be realized through the CEF effect for rare-earth magnetic ion with orbital moment such as in RZn_3P_3 (R = Ce, Pr, Nd, and Sm) system [47,48,50], which deserves further investigation in the future. Given the relatively high AFM transition at $T_N = 4.5$ K, our Hall measurements reveal a clear nonlinear AHE at low carrier density in metallic $GdZn_3P_3$ crystal. In summary, these observations suggest that the $GdZn_3P_3$ system offers a promising platform for investigating the interplay between charge carriers and magnetism in two-dimensional RM_3X_3 compounds.

ACKNOWLEDGMENTS

The authors thank Stephen D. Wilson, Peijie Sun, Junsen Xiang, Xueling Cui, Jiabing Xiang, Gen Li, Qingxin Dong, Huifen Ren, Tao Sun, Bosen Wang, Jie Shen, Shaokui Su, and Jinguang Cheng for helpful discussions and experimental support. The work was supported by the Beijing Natural Science Foundation (Grant No. JQ24012), National Key R&D Program of China (Grants No. 2023YFA1406003, No. 2023YFA1406300, and No. 2022YFA1402604), National Natural Science Foundation of China (Grant No. 12274015 and No. 12174018), and the Fundamental Research Funds for the Central Universities. The authors gratefully acknowledge the scientific and technical support from the Joint Laboratory for Extreme-Condition Physics, Analysis & Testing Center, Beihang University. A portion of this work was carried out at the Synergetic Extreme Condition User Facility (SECUF).

DATA AVAILABILITY

The data that support the findings of this article are not publicly available upon publication because it is not technically feasible and/or the cost of preparing, depositing, and hosting the data would be prohibitive within the terms of this research project. The data are available from the authors upon reasonable request.

[1] L. Balents, Spin liquids in frustrated magnets, Nature (London) **464**, 199 (2010).

[2] C. Broholm, R. J. Cava, S. A. Kivelson, D. G. Nocera, M. R. Norman, and T. Senthil, Quantum spin liquids, Science **367**, eaay0668 (2020).

[3] Y. Li, G. Chen, W. Tong, L. Pi, J. Liu, Z. Yang, X. Wang, and Q. Zhang, Rare-earth triangular lattice spin liquid: A single-crystal study of $YbMgGaO_4$, Phys. Rev. Lett. **115**, 167203 (2015).

[4] Y. Li, D. Adroja, P. K. Biswas, P. J. Baker, Q. Zhang, J. Liu, A. A. Tsirlin, P. Gegenwart, and Q. Zhang, Muon spin relaxation evidence for the U(1) quantum spin-liquid ground state in the triangular antiferromagnet $YbMgGaO_4$, Phys. Rev. Lett. **117**, 097201 (2016).

[5] J. A. M. Paddison, M. Daum, Z. Dun, G. Ehlers, Y. Liu, Matthew B. Stone, H. Zhou, and M. Mourigal, Continuous excitations of the triangular-lattice quantum spin liquid $YbMgGaO_4$, Nat. Phys. **13**, 117 (2016).

[6] Y. Shen, Y.-D. Li, H. Wo, Y. Li, S. Shen, B. Pan, Q. Wang, H. C. Walker, P. Steffens, M. Boehm, Y. Hao, D. L. Quintero-Castro, L. W. Harriger, M. D. Frontzek, L. Hao, S. Meng, Q. Zhang, G. Chen, and J. Zhao, Evidence for a spinon Fermi surface in a triangular-lattice quantum-spin-liquid candidate, Nature (London) **540**, 559 (2016).

[7] Y. Li, D. Adroja, D. Voneshen, R. I. Bewley, Q. Zhang, A. A. Tsirlin, and P. Gegenwart, Nearest-neighbour resonating valence bonds in $YbMgGaO_4$, Nat. Commun. **8**, 15814 (2017).

[8] Y. Li, S. Bachus, B. Liu, I. Radelytskyi, A. Bertin, A. Schneidewind, Y. Tokiwa, A. A. Tsirlin, and P. Gegenwart, Rearrangement of uncorrelated valence bonds evidenced by low-energy spin excitations in $YbMgGaO_4$, Phys. Rev. Lett. **122**, 137201 (2019).

[9] C. Castelnovo, R. Moessner, and S. L. Sondhi, Magnetic monopoles in spin ice, Nature (London) **451**, 42 (2008).

[10] D. J. P. Morris, D. A. Tennant, S. A. Grigera, B. Klemke, C. Castelnovo, R. Moessner, C. Czternasty, M. Meissner, K. C. Rule, J.-U. Hoffmann, K. Kiefer, S. Gerischer, D. Slobinsky, and R. S. Perry, Dirac strings and magnetic monopoles in the spin ice $Dy_2Ti_2O_7$, Science **326**, 411 (2009).

[11] T. Fennell, P. P. Deen, A. R. Wildes, K. Schmalzl, D. Prabhakaran, A. T. Boothroyd, R. J. Aldus, D. F. McMorrow, and S. T. Bramwell, Magnetic coulomb phase in the spin ice $Ho_2Ti_2O_7$, Science **326**, 415 (2009).

[12] G. Möller and R. Moessner, Magnetic multipole analysis of kagome and artificial spin-ice dipolar arrays, Phys. Rev. B **80**, 140409(R) (2009).

[13] G.-W. Chern, P. Mellado, and O. Tchernyshyov, Two-stage ordering of spins in dipolar spin ice on the kagome lattice, Phys. Rev. Lett. **106**, 207202 (2011).

[14] K. Zhao, H. Deng, H. Chen, K. A. Ross, V. Petricek, G. Günther, M. Russina, V. Hutanu, and P. Gegenwart, Realization of the kagome spin ice state in a frustrated intermetallic compound, Science **367**, 1218 (2020).

[15] K. Zhao, Y. Tokiwa, H. Chen, and P. Gegenwart, Discrete degeneracies distinguished by the anomalous Hall effect in a metallic kagome ice compound, Nat. Phys. **20**, 442 (2024).

[16] K. Zhao, H. Deng, H. Chen, N. Ma, N. Oefele, J. Guo, X. Cui, C. Tang, M. J. Gutmann, T. Mueller, Y. Su, V. Hutanu, C. Jin, and P. Gegenwart, Nonlinear time-reversal symmetry breaking in kagome spin ice HoAgGe, arXiv:2505.22544.

[17] Y. Gao, Y.-C. Fan, H. Li, F. Yang, X.-T. Zeng, X.-L. Sheng, R. Zhong, Y. Qi, Y. Wan, and W. Li, Spin supersolidity in nearly ideal easy-axis triangular quantum antiferromagnet $Na_2BaCo(PO_4)_2$, npj Quantum Mater. **7**, 89 (2022).

[18] J. Xiang, C. Zhang, Y. Gao, W. Schmidt, K. Schmalzl, C.-W. Wang, B. Li, N. Xi, X.-Y. Liu, H. Jin, G. Li, J. Shen, Z. Chen, Y. Qi, Y. Wan, W. Jin, W. Li, P. Sun, and G. Su, Giant magnetocaloric effect in spin supersolid candidate $Na_2BaCo(PO_4)_2$, Nature (London) **625**, 270 (2024).

[19] Y. Gao, C. Zhang, J. Xiang, D. Yu, X. Lu, P. Sun, W. Jin, G. Su, and W. Li, Double magnon-roton excitations in the triangular-lattice spin supersolid, Phys. Rev. B **110**, 214408 (2024).

[20] J. Sheng, L. Wang, W. Jiang, H. Ge, N. Zhao, T. Li, M. Kofu, D. Yu, W. Zhu, J.-W. Mei, Z. Wang, and L. Wu, Continuum of spin excitations in an ordered magnet, Innovation **6**, 100769 (2025).

[21] W. Liu, Z. Zhang, J. Ji, Y. Liu, J. Li, X. Wang, H. Lei, G. Chen, and Q. Zhang, Rare-earth chalcogenides: A large family of triangular lattice spin liquid candidates, Chin. Phys. Lett. **35**, 117501 (2018).

[22] J. Xing, L. D. Sanjeewa, J. Kim, W. R. Meier, A. F. May, Q. Zheng, R. Custelcean, G. R. Stewart, and A. S. Sefat, Synthesis, magnetization, and heat capacity of triangular lattice materials $NaErSe_2$ and $KErSe_2$, Phys. Rev. Mater. **3**, 114413 (2019).

[23] P.-L. Dai, G. Zhang, Y. Xie, C. Duan, Y. Gao, Z. Zhu, E. Feng, Z. Tao, C.-L. Huang, H. Cao, A. Podlesnyak, G. E. Granroth, M. S. Everett, J. C. Neuefeind, D. Voneshen, S. Wang, G. Tan, E. Morosan, X. Wang, H.-Q. Lin, L. Shu, G. Chen, Y. Guo, X. Lu, and P. Dai, Spinon fermi surface spin liquid in a triangular lattice antiferromagnet $NaYbSe_2$, Phys. Rev. X **11**, 021044 (2021).

[24] S. Zheng, H. Wo, Y. Gu, R. L. Luo, Y. Gu, Y. Zhu, P. Steffens, M. Boehm, Q. Wang, G. Chen, and J. Zhao, Exchange-renormalized crystal field excitations in the quantum Ising magnet $KTmSe_2$, Phys. Rev. B **108**, 054435 (2023).

[25] A. T. Nientiedt and W. Jeitschko, The series of rare earth zinc phosphides RZn_3P_3 (R = Y, La–Nd, Sm, Gd–Er) and the corresponding cadmium compound $PrCd_3P_3$, J. Solid State Chem. **146**, 478 (1999).

[26] S. S. Stoyko and A. Mar, Ternary rare-earth arsenides $REZn_3As_3$ (RE = La − Nd, Sm) and $RECd_3As_3$ (RE = La − Pr), Inorg. Chem. **50**, 11152 (2011).

[27] Y.-D. Li, X. Wang, and G. Chen, Anisotropic spin model of strong spin-orbit-coupled triangular antiferromagnets, Phys. Rev. B **94**, 035107 (2016).

[28] S. Higuchi, Y. Noshima, N. Shirakawa, M. Tsubota, and J. Kitagawa, Optical, transport and magnetic properties of new compound $CeCd_3P_3$, Mater. Res. Express **3**, 056101 (2016).

[29] N. Kabeya, T. Sakamoto, K. Hara, Y. Hara, S. Nakamura, K. Katoh, and A. Ochiai, Competing exchange interactions in lanthanide triangular lattice compounds $LnZn_3P_3$ (Ln = La − Nd, Sm, Gd), J. Phys. Soc. Jpn. **89**, 074707 (2020).

[30] K. E. Avers, P. A. Maksimov, P. F. S. Rosa, S. M. Thomas, J. D. Thompson, W. P. Halperin, R. Movshovich, and A. L. Chernyshev, Fingerprinting triangular-lattice antiferromagnet by excitation gaps, Phys. Rev. B **103**, L180406 (2021).

[31] Z. Zhou, X. Chen, J.-Y. Lu, J. Zhang, X. Luo, G.-H. Cao, S. Dong, and Z.-C. Wang, Interplay of magnetic ordering and charge transport in distorted $ScAl_3C_3$-type $GdZn_3As_3$, Phys. Rev. B **112**, 054418 (2025).

[32] M. C. Rahn, J. R. Soh, S. Francoual, L. S. I. Veiga, J. Strempfer, J. Mardegan, D. Y. Yan, Y. F. Guo, Y. G. Shi, and A. T. Boothroyd, Coupling of magnetic order and charge transport in the candidate Dirac semimetal $EuCd_2As_2$, Phys. Rev. B **97**, 214422 (2018).

[33] J. R. Soh, F. de Juan, M. G. Vergniory, N. B. M. Schröter, M. C. Rahn, D. Y. Yan, J. Jiang, M. Bristow, P. Reiss, J. N. Blandy, Y. F. Guo, Y. G. Shi, T. K. Kim, A. McCollam, S. H. Simon, Y. Chen, A. I. Coldea, and A. T. Boothroyd, Ideal Weyl semimetal induced by magnetic exchange, Phys. Rev. B **100**, 201102(R) (2019).

[34] N. H. Jo, B. Kuthanazhi, Y. Wu, E. Timmons, T.-H. Kim, L. Zhou, L.-L. Wang, B. G. Ueland, A. Palasyuk, D. H. Ryan, R. J. McQueeney, K. Lee, B. Schrunk, A. A. Burkov, R. Prozorov, S. L. Bud'ko, A. Kaminski, and P. C. Canfield, Manipulating magnetism in the topological semimetal $EuCd_2As_2$, Phys. Rev. B **101**, 140402(R) (2020).

[35] B. Kuthanazhi, K. R. Joshi, S. Ghimire, E. Timmons, L.-L. Wang, E. Gati, L. Xiang, R. Prozorov, S. L. Bud'ko, and P. C. Canfield, Magnetism and T−x phase diagrams of Na- and Ag-substituted $EuCd_2As_2$, Phys. Rev. Mater. **7**, 034402 (2023).

[36] Y. Wang, C. Li, Y. Li, X. Zhou, W. Wu, R. Yu, J. Zhao, C. Yin, Y. Shi, C. Jin, J. Luo, L. Zhao, T. Xiang, G. Liu, and X. J. Zhou, Long-time magnetic relaxation in antiferromagnetic topological material $EuCd_2As_2$, Chin. Phys. Lett. **38**, 077201 (2021).

[37] X. Cao, J.-X. Yu, P. Leng, C. Yi, X. Chen, Y. Yang, S. Liu, L. Kong, Z. Li, X. Dong, Y. Shi, M. Bibes, R. Peng, J. Zang, and F. Xiu, Giant nonlinear anomalous Hall effect induced by spin-dependent band structure evolution, Phys. Rev. Res. **4**, 023100 (2022).

[38] Y. Shi, Z. Liu, L. A. Burnett, S. Lee, C. Hu, Q. Jiang, J. Cai, X. Xu, M. Li, C.-C. Chen, and J.-H. Chu, Absence of Weyl nodes

in $EuCd_2As_2$ revealed by the carrier density dependence of the anomalous Hall effect, Phys. Rev. B **109**, 125202 (2024).

[39] Z.-C. Wang, E. Been, J. Gaudet, Gadeer Matook A. Alqasseri, K. Fruhling, X. Yao, U. Stuhr, Q. Zhu, Z. Ren, Y. Cui, C. Jia, B. Moritz, S. Chowdhury, T. Devereaux, and F. Tafti, Anisotropy of the magnetic and transport properties of $EuZn_2As_2$, Phys. Rev. B **105**, 165122 (2022).

[40] T. Berry, V. J. Stewart, Benjamin W. Y. Redemann, C. Lygouras, N. Varnava, D. Vanderbilt, and T. M. McQueen, A-type antiferromagnetic order in the Zintl-phase insulator $EuZn_2P_2$, Phys. Rev. B **106**, 054420 (2022).

[41] K. Singh, S. Dan, A. Ptok, T. A. Zaleski, O. Pavlosiuk, P. Wiśniewski, and D. Kaczorowski, Superexchange interaction in insulating $EuZn_2P_2$, Phys. Rev. B **108**, 054402 (2023).

[42] S. Krebber, M. Kopp, C. Garg, K. Kummer, J. Sichelschmidt, S. Schulz, G. Poelchen, M. Mende, A. V. Virovets, K. Warawa, M. D. Thomson, A. V. Tarasov, D. Y. Usachov, D. V. Vyalikh, H. G. Roskos, J. Müller, C. Krellner, and K. Kliemt, Colossal magnetoresistance in $EuZn_2P_2$ and its electronic and magnetic structure, Phys. Rev. B **108**, 045116 (2023).

[43] S. Luo, Y. Xu, F. Du, L. Yang, Y. Chen, C. Cao, Y. Song, and H. Yuan, Colossal magnetoresistance and topological phase transition in $EuZn_2As_2$, Phys. Rev. B **108**, 205140 (2023).

[44] X. Chen, W. Yang, J.-Y. Lu, Z. Zhou, Z. Ren, G.-H. Cao, S. Dong, and Z.-C. Wang, Carrier-induced transition from antiferromagnetic insulator to ferromagnetic metal in the layered phosphide $EuZn_2P_2$, Phys. Rev. B **109**, L180410 (2024).

[45] D. Rybicki, K. Komędera, J. Przewoźnik, Ł. Gondek, C. Kapusta, K. Podgórska, W. Tabiś, J. Żukrowski, L. M. Tran, M. Babij, Z. Bukowski, L. Havela, V. Buturlim, J. Prchal, M. Divis, P. Kral, I. Turek, I. Halevy, J. Kastil, M. Misek, U. Dutta, and D. Legut, Ambient- and high-pressure studies of structural, electronic, and magnetic properties of single-crystal $EuZn_2P_2$, Phys. Rev. B **110**, 014421 (2024).

[46] O. P. Uzoh, S. Kim, and E. Mun, Influence of crystalline electric field on the magnetic properties of $CeCd_3X_3$ (X = P, As), Phys. Rev. Mater. **7**, 013402 (2023).

[47] J. Lee, A. Rabus, N. R. Lee-Hone, D. M. Broun, and E. Mun, The two-dimensional metallic triangular lattice antiferromagnet $CeCd_3P_3$, Phys. Rev. B **99**, 245159 (2019).

[48] S. R. Dunsiger, J. Lee, J. E. Sonier, and E. D. Mun, Long-range magnetic order in the anisotropic triangular lattice system $CeCd_3As_3$, Phys. Rev. B **102**, 064405 (2020).

[49] J. R. Chamorro, A. R. Jackson, A. K. Watkins, R. Seshadri, and S. D. Wilson, Magnetic order in the $S_{eff} = 1/2$ triangular-lattice compound $NdCd_3P_3$, Phys. Rev. Mater. **7**, 094402 (2023).

[50] J. R. Chamorro, Steven J. Gomez. Alvarado, D. Rout, S. Schwarz, A. Scheie, G. Pokharel, A. I. Kolesnikov, L. Keller, and S. D. Wilson, Hidden frustration in the triangular-lattice antiferromagnet $NdCd_3P_3$, Phys. Rev. Mater. **9**, 104414 (2025).

[51] A. Ochiai, N. Kabeya, K. Maniwa, M. Saito, S. Nakamura, and K. Katoh, Field-induced anomalous magnetic state beyond the magnetically ordered state in the slightly distorted triangular $S = 12$ rare-earth antiferromagnet $CeZn_3P_3$, Phys. Rev. B **104**, 144420 (2021).

[52] S. J. Gomez Alvarado, J. R. Chamorro, D. Rout, J. Hielscher, S. Schwarz, C. Benyacko, M. B. Stone, V. O. Garlea, A. R. Jackson, G. Pokharel, R. Gomez, B. R. Ortiz, S. Sarker, L. Kautzsch, L. C. Gallington, R. Seshadri, and S. D. Wilson, Interleaved bond frustration in a triangular lattice antiferromagnet, Nat. Mater. **25**, 65 (2026).

[53] See Supplemental Material at http://link.aps.org/supplemental/10.1103/qfbt-xn97 for additional details about x-ray diffraction, STEM, magnetization, DFT results, and photographs of the samples mounted on the transport puck, which includes Ref. [54].

[54] A. Jain, S. P. Ong, G. Hautier, W. Chen, W. D. Richards, S. Dacek, S. Cholia, D. Gunter, D. Skinner, G. Ceder, and K. A. Persson, Commentary: The Materials Project: A materials genome approach to accelerating materials innovation, APL Mater. **1**, 011002 (2013).

[55] O. V. Dolomanov, L. J. Bourhis, R. J. Gildea, J. A. K. Howard, and H. Puschmann, OLEX2 : A complete structure solution, refinement and analysis program, J. Appl. Crystallogr. **42**, 339 (2009).

[56] G. M. Sheldrick, A short history of SHELX, Acta Crystallogr., Sect. A:Found. Crystallogr. **64**, 112 (2007).

[57] A. D. Becke, Density-functional exchange-energy approximation with correct asymptotic behavior, Phys. Rev. A **38**, 3098 (1988).

[58] J. P. Perdew, J. A. Chevary, S. H. Vosko, K. A. Jackson, M. R. Pederson, D. J. Singh, and C. Fiolhais, Atoms, molecules, solids, and surfaces: Applications of the generalized gradient approximation for exchange and correlation, Phys. Rev. B **46**, 6671 (1992).

[59] J. P. Perdew, K. Burke, and M. Ernzerhof, Generalized gradient approximation made simple, Phys. Rev. Lett. **77**, 3865 (1996).

[60] G. Kresse and J. Hafner, *Ab initio* molecular dynamics for liquid metals, Phys. Rev. B **47**, 558 (1993).

[61] G. Kresse and J. Furthmüller, Efficiency of *ab-initio* total energy calculations for metals and semiconductors using a plane-wave basis set, Comput. Mater. Sci. **6**, 15 (1996).

[62] G. Kresse and J. Furthmüller, Efficient iterative schemes for *ab initio* total-energy calculations using a plane-wave basis set, Phys. Rev. B **54**, 11169 (1996).

[63] K. Zhao, E. Golias, Q. H. Zhang, M. Krivenkov, A. Jesche, L. Gu, O. Rader, I. I. Mazin, and P. Gegenwart, Quantum oscillations and Dirac dispersion in the $BaZnBi_2$ semimetal guaranteed by local Zn vacancy order, Phys. Rev. B **97**, 115166 (2018).

[64] T. Matsumura, T. Inami, M. Kosaka, Y. Kato, T. Inukai, A. Ochiai, H. Nakao, Y. Murakami, S. Katano, and H. S. Suzuki, Structural Phase Transition in the Spin Gap System $YbAl_3C_3$, J. Phys. Soc. Jpn. **77**, 103601 (2008).

[65] G. Pokharel, Samuel M. L. Teicher, B. R. Ortiz, P. M. Sarte, G. Wu, S. Peng, J. He, R. Seshadri, and S. D. Wilson, Electronic properties of the topological kagome metals YV_6Sn_6 and GdV_6Sn_6, Phys. Rev. B **104**, 235139 (2021).

[66] Z. Porter, G. Pokharel, J.-W. Kim, P. J. Ryan, and S. D. Wilson, Incommensurate magnetic order in the Z_2 kagome metal GdV_6Sn_6, Phys. Rev. B **108**, 035134 (2023).

[67] Z. Y. Yang, H. H. Zhang, M. J. Bai, W. Li, S. L. Huang, S. C. Ruan, and Y. J. Zeng, Large magnetocaloric effect in gadolinium borotungstate Gd_3BWO_9, J. Mater. Chem. C **8**, 11866 (2020).

[68] Z. Wang, X. Cui, T. Treu, J. Guo, X. Liu, M. Klinger, C. Heil, N. Ma, X. Sheng, Z. Deng, X. Lu, X. Wang, W. Li, P. Gegenwart, C. Jin, and K. Zhao, Antiferromagnetic ordering and critical behavior induced giant magnetocaloric effect in distorted kagome lattice Gd_3BWO_9, Phys. Rev. Mater. **9**, 094407 (2025).

[69] Z. W. Yang, J. Zhang, B. Liu, X. Zhang, D. Lu, H. Zhao, M. Pi, H. Cui, Y. J. Zeng, Z. Pan, Y. Shen, S. Li, and Y. Long, Exceptional magnetocaloric responses in a gadolinium silicate with strongly correlated spin disorder for sub-kelvin magnetic cooling, Adv. Sci. **11**, 2306842 (2024).

[70] K. Singh, O. Pavlosiuk, S. Dan, D. Kaczorowski, and P. Wiśniewski, Large unconventional anomalous Hall effect arising from spin chirality within domain walls of an antiferromagnet $EuZn_2Sb_2$, Phys. Rev. B **109**, 125107 (2024).

[71] L. Zhang, Z. Sun, A. Wang, Y. Xia, X. Mi, L. Zhang, M. He, Y. Chai, T. Wu, R. Wang, X. Zhou, and X. Chen, Strong coupling between magnetic order and band topology in the antiferromagnet $EuMnSb_2$, Phys. Rev. B **104**, 205108 (2021).

[72] J. M. Wilde, S. X. M. Riberolles, A. Das, Y. Liu, T. W. Heitmann, X. Wang, W. E. Straszheim, S. L. Bud'ko, P. C. Canfield, A. Kreyssig, R. J. McQueeney, D. H. Ryan, and B. G. Ueland, Canted antiferromagnetic phases in the candidate layered Weyl material $EuMnSb_2$, Phys. Rev. B **106**, 024420 (2022).

[73] K. Zhao, X. Chen, Z. Wang, J. Liu, J. Wu, C. Xi, X. Lv, L. Li, Z. Zhong, and P. Gegenwart, Magnetic tuning of band topology evidenced by exotic quantum oscillations in the Dirac semimetal $EuMnSb_2$, Phys. Rev. B **107**, L081112 (2023).